

**1 Temporal Structures in Positron Spectra and Charge Sign Effects**  
**2 in Galactic Cosmic Rays**  
**3 - SUPPLEMENTAL MATERIAL -**

**4 (AMS Collaboration)**

5 For references see the main text.

6 *Detector.*—AMS is a general purpose high energy particle physics detector in space. The  
7 layout of the detector is shown in Fig. S1. The main elements are the permanent magnet,  
8 the silicon tracker, four planes of time of flight (TOF) scintillation counters, the array of  
9 anticoincidence counters (ACCs), a transition radiation detector (TRD), a ring imaging  
10 Čerenkov detector (RICH), and an electromagnetic calorimeter (ECAL).

11 The AMS coordinate system is concentric with the magnet. The  $x$  axis is parallel to the  
12 main component of the magnetic field and the  $z$  axis points vertically with  $z = 0$  at the  
13 center of the magnet. The ( $y$ - $z$ ) plane is the bending plane. Above, below, and downward-  
14 going refer to the AMS coordinate system. The central field of the magnet is 1.4 kG. Before  
15 flight, the field was measured in 120 000 locations to an accuracy of better than 2 G. On  
16 orbit, the magnet temperature varies from  $-3$  to  $+20^\circ\text{C}$ . The field strength is corrected with  
17 a measured temperature dependence of  $-0.09\%/^\circ\text{C}$ .

18 The tracker has nine layers, the first ( $L1$ ) at the top of the detector, the second ( $L2$ )  
19 just above the magnet, six ( $L3$  to  $L8$ ) within the bore of the magnet, and the last ( $L9$ ) just  
20 above the ECAL.  $L2$  to  $L8$  constitute the inner tracker. Each layer contains double-sided  
21 silicon microstrip detectors which independently measure the  $x$  and  $y$  coordinates. The  
22 tracker accurately determines the trajectory of cosmic rays by multiple measurements of  
23 the coordinates with a resolution in each layer of  $10\ \mu\text{m}$  for  $|Z|=1$  particles in the bending  
24 ( $y$ ) direction. Together, the tracker and the magnet measure the rigidity of charged cosmic  
25 rays. Each layer of the tracker provides an independent measurement of charge  $Z$  with a  
26 resolution of  $\sigma_Z = 0.092$  charge units for  $|Z|=1$  particles. Overall, the inner tracker has a  
27 resolution of  $\sigma_Z = 0.049$  charge units for  $|Z|=1$  particles.

28 Two TOF planes are located above the magnet (upper TOF) and two planes are below  
29 the magnet (lower TOF). The overall velocity ( $\beta = v/c$ ) resolution has been measured to be  
30  $\sigma(1/\beta) = 0.04$  for  $|Z|=1$  particles. This discriminates between upward- and downward-going  
31 particles. The pulse heights of the two upper planes are combined to provide an independent  
32 measurement of the charge with an accuracy  $\sigma_Z = 0.06$  charge units for  $|Z|=1$  particles.  
33 The pulse heights from the two lower planes are combined to provide another independent  
34 charge measurement with the same accuracy.

35 The TRD separates  $e^+$  from protons using a  $\Lambda_{\text{TRD}}$  estimator constructed from the ratio  
36 of the log-likelihood probability of the  $e^\pm$  hypothesis to that of the  $p$  hypothesis in each  
37 layer [19].

38 The three dimensional imaging capability of the 17 radiation length ECAL allows for an  
39 accurate measurement of the positron energy and of the shower shape. The  $e^\pm$  energy,  $E$ ,  
40 is calibrated at the top of AMS. An ECAL estimator  $\Lambda_{\text{ECAL}}$  [19] is used to differentiate  $e^\pm$   
41 from  $p$  by exploiting their different shower shapes.

42 Positrons traversing AMS were triggered as described in Ref. [19]. The trigger efficiency  
43 is 100% above 3 GV, decreasing to 83% at 1 GV, and is stable over time within errors.

44 Monte Carlo simulated events were produced using a dedicated program developed by  
45 the collaboration based on the GEANT4-10.3 package [30]. The program simulates elec-  
46 tromagnetic and hadronic interactions of particles in the material of AMS and generates  
47 detector responses. The digitization of the signals is simulated precisely according to the  
48 measured characteristics of the electronics. The simulated events then undergo the same  
49 reconstruction as used for the data.

50 *Event Selection.*—AMS has collected  $1.9 \times 10^{11}$  cosmic ray events from May 20, 2011 to  
51 November 2, 2021. The collection time used includes only those seconds during which the

52 detector was in normal operating conditions and, in addition, AMS was pointing within  $40^\circ$   
53 of the local zenith and the ISS was outside of the South Atlantic Anomaly. Because of the  
54 geomagnetic field, the daily collection time  $T_i^j$  of the positron fluxes,  $\Phi_{e^+}$ , increases with  
55 rigidity and is  $(1.3 - 3.2) \times 10^3$  s at 1 GV,  $(4.0 - 7.3) \times 10^3$  s at 2 GV,  $(1.6 - 2.2) \times 10^4$  s at  
56 5 GV,  $(2.9 - 3.7) \times 10^4$  s at 10 GV,  $(5.4 - 6.6) \times 10^4$  s at 20 GV, and, above 30 GV, reaches  
57  $(6.0 - 7.2) \times 10^4$  s.

58 Positron events are required to be downward going ( $\beta > 0.8$ ), to have a reconstructed  
59 shower in the ECAL with a matched track in the tracker and the TRD. The track is required  
60 to pass through either  $L1$ ,  $L2$  or  $L9$ . Track fitting quality criteria such as a  $\chi^2/\text{d.o.f.} < 10$   
61 both in the bending and non-bending planes are applied to ensure good accuracy of the  
62 track reconstruction. The charge measurements in the TOF and the tracker are required to  
63 be consistent with  $|Z|=1$ .

64 In this Letter, the ECAL energy is used to calculate the positron absolute rigidity  $R$ . The  
65 rigidity is required to be greater than the local geomagnetic cutoff. The local geomagnetic  
66 cutoff was calculated as the maximum geomagnetic cutoff within the AMS field of view  
67 from AMS data by measuring the proton flux at each geomagnetic position. The details  
68 of this study will be included in a future publication [31]. To estimate the associated  
69 systematic error, we increase the calculated value of the geomagnetic cutoff by 10%. This  
70 results in a systematic error on the fluxes of  $< 2\%$  at 1 GV reducing to a negligible level  
71 ( $< 0.4\%$ ) above 2 GV. We have verified that using a geomagnetic cutoff derived from the  
72 most recent International Geomagnetic Reference Field (IGRF) model [32] with external  
73 non-symmetric magnetic fields [33] during the most disturbed geomagnetic periods does not  
74 introduce observable changes in the flux values nor in the systematic errors.

75 Events satisfying the above criteria are classified into two categories: positive and negative  
76 rigidity data samples. In this Letter we only consider the positive rigidity data sample,  
77 which comprises mostly positrons, background protons, and charge confusion electrons, that  
78 is, electrons that are reconstructed in the tracker with positive rigidity due to the finite  
79 tracker resolution or due to interactions with the detector materials.

80 The combination of information from the TRD, tracker, and ECAL enables the efficient  
81 separation of the positron signal events from these background sources for each rigidity bin  
82 on a daily basis. A cut on  $\Lambda_{\text{ECAL}}$  is applied to remove the bulk of the proton background.  
83 The residual proton background contribution is  $\sim 1\%$  in the positron signal region and is  
84 estimated using a template fit to the TRD estimator  $\Lambda_{\text{TRD}}$ . The electron background is  
85 estimated from the Monte Carlo simulation by accounting for the daily variation of the  $\Phi_{e^-}$ .  
86 It amounts to  $\sim 1\%$  of the positron signal over the entire rigidity range. After background  
87 subtraction,  $3.4 \times 10^6$  positrons are identified in the rigidity range from 1.00 to 41.9 GV.

TABLE SA. The range of each year from 2011 to 2021 in BRs and dates.

Year	Range [BR]	Range [Date]
2011	2426 – 2433	May 20, 2011 – December 16, 2011
2012	2434 – 2447	December 17, 2011 – December 28, 2012
2013	2448 – 2461	December 29, 2012 – January 10, 2014
2014	2462 – 2471	January 11, 2014 – September 29, 2014
2015	2473 – 2488	November 29, 2014 – January 9, 2016
2016	2489 – 2502	January 10, 2016 – January 21, 2017
2017	2503 – 2515	January 22, 2017 – January 7, 2018
2018	2516 – 2528	January 8, 2018 – December 24, 2018
2019	2529 – 2540	December 25, 2018 – October 29, 2019
2020	2543 – 2554	January 26, 2020 – November 18, 2020
2021	2554 – 2567	November 19, 2020 – November 2, 2021

88 *Wavelet Analysis.*—The continuous wavelet transform  $W_n$  of a time series  $x_n$  with equal  
 89 time interval  $\delta t$  is defined as [36]:

$$W_n(s) = \sum_{n'=1}^N x_{n'} \psi^* \left[ \frac{(n' - n)\delta t}{s} \right], \quad (\text{S1})$$

90 where the  $*$  indicates the complex conjugate of the wavelet function  $\psi$ ,  $s$  is the period, and  
 91  $n$  is the time index of the wavelet. In this study, we chose the Morlet wavelet, consisting of  
 92 a plane wave modulated by a Gaussian:

$$\psi(\eta) = \pi^{-1/4} e^{i6\eta} e^{-\eta^2/2}, \quad (\text{S2})$$

93 where  $\eta$  is a nondimensional time parameter. The wavelet power is given by  $|W_n(s)|^2$ . The  
 94 wavelet time-frequency power spectrum shows the temporal distribution of the power for  
 95 each period  $s$ . The time-averaged power spectrum over a certain time interval is

$$\overline{W}_n^2(s) = \frac{1}{n_2 - n_1 + 1} \sum_{n=n_1}^{n_2} |W_n(s)|^2, \quad (\text{S3})$$

96 where  $n_1$  and  $n_2$  are the beginning and ending indexes of the analyzed time interval, respec-  
 97 tively.

98 In both the wavelet time-frequency power spectrum and time-averaged power spectrum,  
 99 the normalized power is defined by the wavelet power divided by the variance  $\sigma^2$  of the time  
 100 series  $x_n$  in the corresponding time interval:

$$\sigma^2 = \frac{\sum_{n=n_1}^{n_2} (x_n - \bar{x})^2}{n_2 - n_1}, \quad (\text{S4})$$

101 where  $\bar{x}$  is the mean value of the time series. This normalization by variance is applied to  
 102 show the strength of the periodicities.

103 To determine significance levels above which the power represents periodic structures,  
 104 Monte Carlo simulations are used to assess the statistical significance against backgrounds  
 105 which are generated by the lag-1 autoregressive process [36]:

$$y_n = \alpha y_{n-1} + z_n, \quad (\text{S5})$$

106 where  $z_n$  is a Gaussian with zero mean and width such that the variance of the simulated  
 107 time series is equal to the measured time series. Here,  $\alpha$  is the lag-1 autocorrection obtained  
 108 from the measured time series  $x_n$ :

$$\alpha = \frac{\sum_{n=1}^{N-1} (x_n - \bar{x})(x_{n+1} - \bar{x})}{\sum_{n=1}^N (x_n - \bar{x})^2}, \quad (\text{S6})$$

109 where  $N$  is the number of measured points and  $\bar{x}$  is the mean value of the time series.

110 For each period, the 95% confidence level is determined by the power exceeded by 5% of  
 111 the power values calculated from the simulated background. The 95% confidence level has  
 112 different shapes due to different solar modulation effects as a function of rigidity.

113 *Hysteresis Analysis.*—The hysteresis occurs over the time span from 2011 to 2018 as  
 114 seen in Fig. 2(c) and Fig. S16. To analyze the significance of the hysteresis, we select the  
 115 two time intervals with the same electron flux,  $\Phi_{e^-}$ , one before 2014-2015 and one after,  
 116 with the most significant difference in  $\Phi_{e^+}$ . From this, we determine that the maximum  
 117 difference in the rigidity range from 1.00 to 1.71 GV is at  $\Phi_{e^-} = 13.89 \text{ m}^{-2}\text{sr}^{-1}\text{s}^{-1}\text{GV}^{-1}$   
 118 which occurs in 2013 and 2016 (points A and B in Fig. S16(a), with positron fluxes  $\Phi_{e^+}^A$  and  
 119  $\Phi_{e^+}^B$  respectively). The variation in the positron flux is  $\Phi_{e^+}^B/\Phi_{e^+}^A = 1.754 \pm 0.044$ . The errors  
 120 in both  $\Phi_{e^+}$  and  $\Phi_{e^-}$  are accounted for in the error calculation of the ratio. To obtain the  
 121 overall significance of the hysteresis, we repeat the procedure for remaining non-overlapping  
 122 time intervals and determine that the maximum difference for these remaining intervals  
 123 is at  $\Phi_{e^-} = 19.71 \text{ m}^{-2}\text{sr}^{-1}\text{s}^{-1}\text{GV}^{-1}$  which occurs in 2011 and 2018 (points C and D in  
 124 Fig. S16(a), with positron fluxes  $\Phi_{e^+}^C$  and  $\Phi_{e^+}^D$  respectively). The variation in the positron  
 125 flux is  $\Phi_{e^+}^D/\Phi_{e^+}^C = 1.711 \pm 0.042$ . The analysis is repeated for the rest of the rigidity bins,  
 126 see Fig. S16(b-f).

127 Figure S17 shows the evaluated positron flux ratios  $\Phi_{e^+}^B/\Phi_{e^+}^A$  and  $\Phi_{e^+}^D/\Phi_{e^+}^C$  as a function  
 128 of rigidity. As seen, the difference in  $\Phi_{e^+}$  decreases with increasing rigidity. In particular, at  
 129 [7.09–8.48] GV, with  $\Phi_{e^+}^B/\Phi_{e^+}^A = 1.066 \pm 0.020$  and  $\Phi_{e^+}^D/\Phi_{e^+}^C = 1.107 \pm 0.021$ , the combined  
 130 significance of the difference in  $\Phi_{e^+}$  before and after 2014-2015 is  $5.7\sigma$ . At [8.48 – 11.0] GV,  
 131 with  $\Phi_{e^+}^B/\Phi_{e^+}^A = 1.062 \pm 0.024$  and  $\Phi_{e^+}^D/\Phi_{e^+}^C = 1.049 \pm 0.020$ , the combined significance of  
 132 the difference in  $\Phi_{e^+}$  before and after 2014-2015 is  $3.1\sigma$ .

133 In summary, the hysteresis is observed with a significance greater than  $5\sigma$  below 8.48 GV  
 134 and with  $3.1\sigma$  at [8.48 – 11.0] GV.

135 *Hysteresis Structures Analysis.*— The hysteresis exhibits structures during the flux dips  
 136 in 2015 and 2017, see Fig. 3 and S18 for the rigidity range from 1.00 to 1.71 GV. To analyze  
 137 the significance of the hysteresis structures in 2015, we select the two time intervals with the  
 138 same  $\Phi_{e^+}$ , one in the first half (E) and one in the second half (F) of region IV, with electron  
 139 fluxes  $\Phi_{e^-}^E$  and  $\Phi_{e^-}^F$  respectively, which show the most significant difference in  $\Phi_{e^-}$ . From  
 140 this, we determine that the maximum difference for the rigidity interval [1.00–1.71] GV is at  
 141  $\Phi_{e^+} = 0.965 \text{ m}^{-2}\text{sr}^{-1}\text{s}^{-1}\text{GV}^{-1}$  and the variation in electron flux is  $\Phi_{e^-}^F/\Phi_{e^-}^E = 0.844 \pm 0.018$ ,  
 142 see Fig. S18(c). The errors in both  $\Phi_{e^-}$  and  $\Phi_{e^+}$  are accounted for in the error calculation  
 143 of the ratio. To obtain the overall significance of the hysteresis structure, we repeat the  
 144 procedure for remaining non-overlapping time intervals of region IV and determine that the  
 145 maximum difference for [1.00–1.71] GV is at  $\Phi_{e^+} = 1.197 \text{ m}^{-2}\text{sr}^{-1}\text{s}^{-1}\text{GV}^{-1}$ , indicated as  
 146 G and H in Fig. S18(c), with electron fluxes  $\Phi_{e^-}^G$  and  $\Phi_{e^-}^H$  respectively. The variation in  
 147 electron flux is  $\Phi_{e^-}^H/\Phi_{e^-}^G = 0.845 \pm 0.027$ . Both  $\Phi_{e^-}^F/\Phi_{e^-}^E$  and  $\Phi_{e^-}^H/\Phi_{e^-}^G$  deviate from unity.  
 148 The overall significance of the hysteresis structure corresponding to the dip in 2015 is  $10\sigma$ .  
 149 The analysis is repeated for the dip in 2017 (V), as shown in Fig. S18(d), with the four  
 150 corresponding points J, K, L, M, with electron fluxes  $\Phi_{e^-}^J$ ,  $\Phi_{e^-}^K$ ,  $\Phi_{e^-}^L$ , and  $\Phi_{e^-}^M$  respectively.  
 151 The variation in electron flux is  $\Phi_{e^-}^J/\Phi_{e^-}^K = 0.910 \pm 0.032$  for  $\Phi_{e^+} = 2.423 \text{ m}^{-2}\text{sr}^{-1}\text{s}^{-1}\text{GV}^{-1}$ ,  
 152 and  $\Phi_{e^-}^L/\Phi_{e^-}^M = 0.928 \pm 0.022$  for  $\Phi_{e^+} = 2.710 \text{ m}^{-2}\text{sr}^{-1}\text{s}^{-1}\text{GV}^{-1}$ . The significance of the  
 153 corresponding hysteresis structure is  $4\sigma$ .

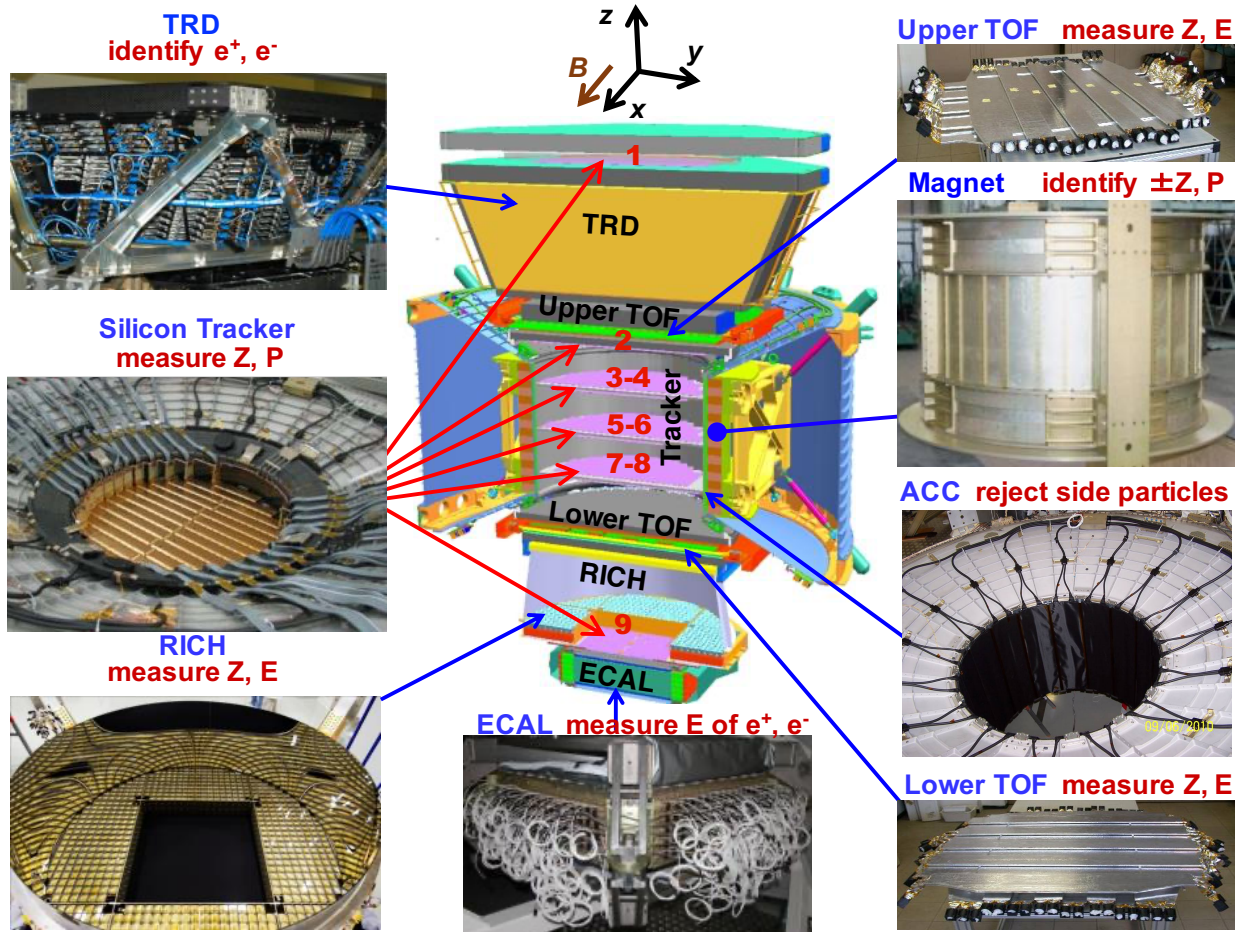


FIG. S1. The AMS detector showing the main elements and their functions. AMS is a TeV precision, multipurpose particle physics magnetic spectrometer in space. It identifies particles and nuclei by their charge  $Z$ , energy  $E$ , and momentum  $P$  or rigidity ( $R = P/Z$ ), which are measured independently by the Tracker, TOF, RICH and ECAL. The ACC counters, located in the magnet bore, are used to reject particles entering AMS from the side. The AMS coordinate system is also shown. The  $x$  axis is parallel to the main component of the magnetic field and the  $z$  axis points vertically with  $z = 0$  at the center of the magnet.

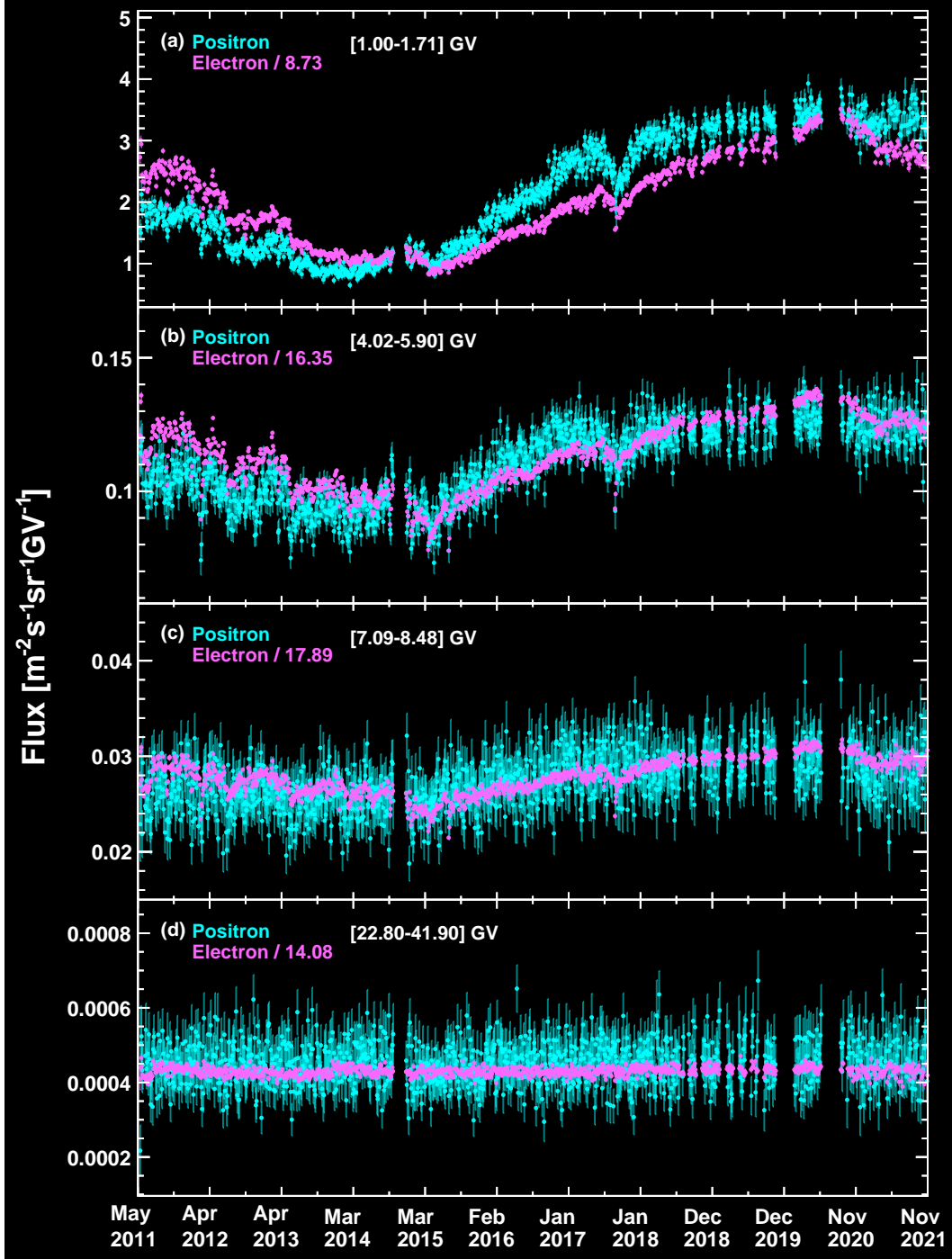


FIG. S2. The 3-day averaged  $\Phi_{e+}$  (light blue points) together with the 3-day averaged  $\Phi_{e-}$  (magenta points), measured over the entire period for four rigidity bins from 1.00 to 41.9 GV. The gaps in the fluxes are due to detector studies and upgrades.  $\Phi_{e-}$  are divided by different scale factors as indicated. The scale factors are chosen such that  $\Phi_{e-}$  and  $\Phi_{e+}$  for each rigidity bin are at the same magnitude on average during 2014 and 2015. As seen,  $\Phi_{e+}$  exhibits short-term variations on the scale of days to months, and long-term variations on the scale of years, and the relative magnitude of these variations decreases with increasing rigidity. Below 8.5 GV, (abc),  $\Phi_{e+}$  decreases more slowly with time than  $\Phi_{e-}$  from 2011 to 2014, rises more quickly from 2014 to 2017, rises more slowly from 2017 to mid-2020, and again, decreases more slowly from mid-2020 to 2021. In the rigidity range [22.8-41.9] GV (d), the difference between the time evolution of  $\Phi_{e+}$  and  $\Phi_{e-}$  becomes negligible.

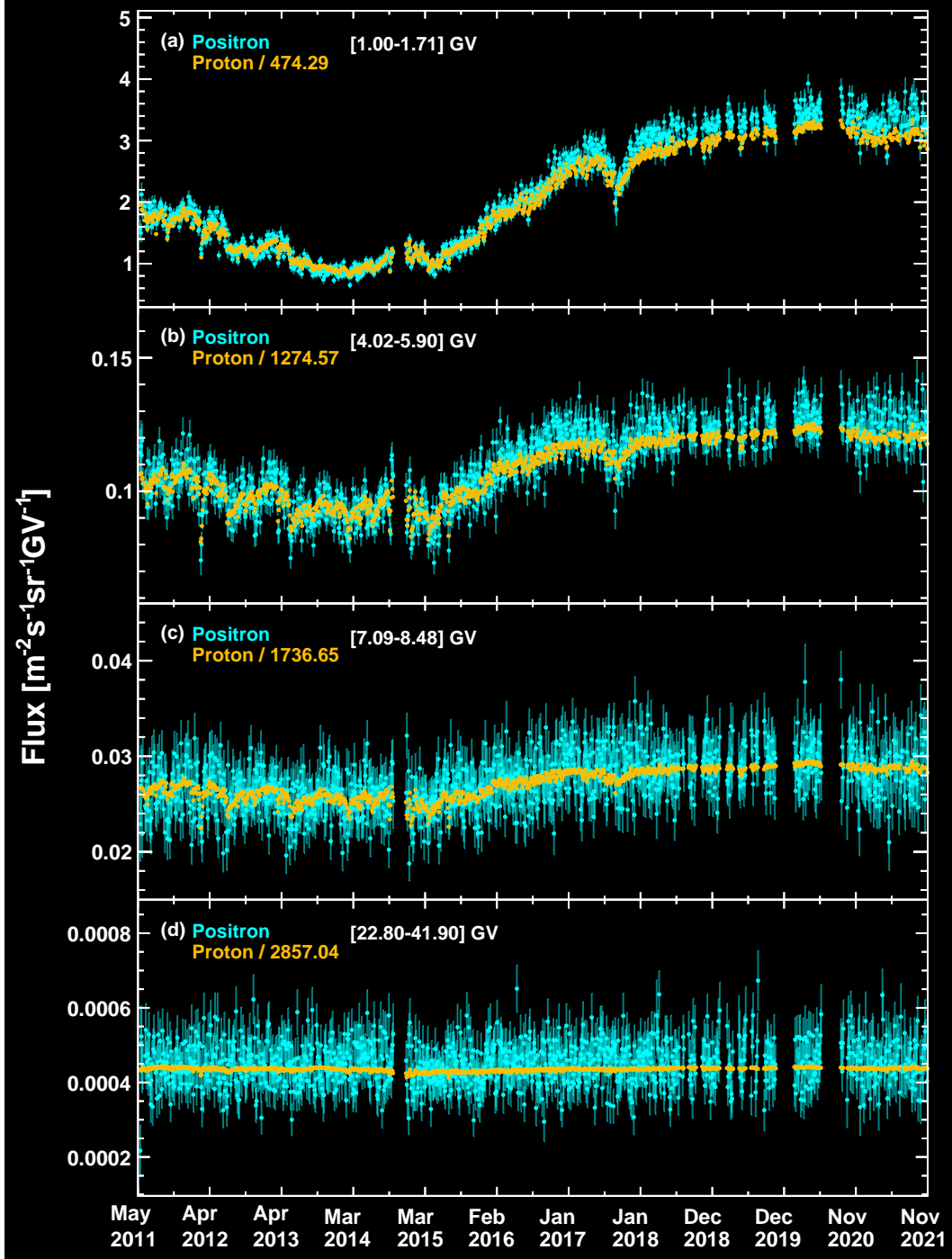


FIG. S3. The 3-day averaged  $\Phi_{e^+}$  (light blue points) together with the 3-day averaged  $\Phi_p$  (yellow points), measured over the entire period for four rigidity bins from 1.00 to 41.9 GV. Days with Solar Energetic Particle events are excluded from  $\Phi_p$ . The gaps in the fluxes are due to detector studies and upgrades.  $\Phi_p$  are divided by different scale factors as indicated. The scale factors are chosen such that  $\Phi_{e^+}$  and  $\Phi_p$  for each rigidity bin are at the same magnitude on average during 2014 and 2015. As seen, both fluxes present a similar behavior with time in short-term and long-term timescales, and at low rigidity (ab),  $\Phi_{e^+}$  exhibits a larger variation than  $\Phi_p$ . At higher rigidities (c), the difference in their respective time evolution decreases and becomes negligible in the rigidity range [22.8-41.9] GV (d).

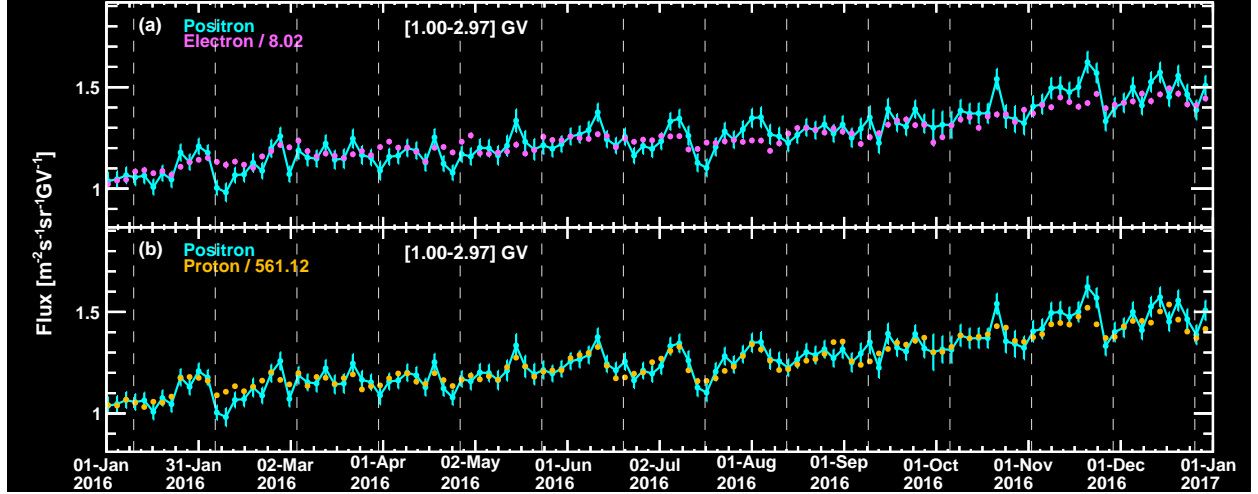


FIG. S4. The 3-day averaged  $\Phi_{e+}$  (light blue points) in the rigidity range from 1.00 to 2.97 GV, measured from January 1, 2016 to January 1, 2017 together with (a) 3-day averaged  $\Phi_{e-}$  (magenta points) and (b) 3-day averaged  $\Phi_p$  (yellow points) in the same rigidity range and time period. Vertical dashed lines separate Bartels rotations.  $\Phi_{e-}$  and  $\Phi_p$  are divided by different scale factors chosen such that  $\Phi_{e+}$ ,  $\Phi_{e-}$ , and  $\Phi_p$  are at the same magnitude on average. The contiguous  $\Phi_{e+}$  data points are connected with lines to guide the eye. As seen in (a),  $\Phi_{e+}$  shows time variations that are different from those observed in  $\Phi_{e-}$ . On the contrary (b),  $\Phi_{e+}$  and  $\Phi_p$  show similar time variations.

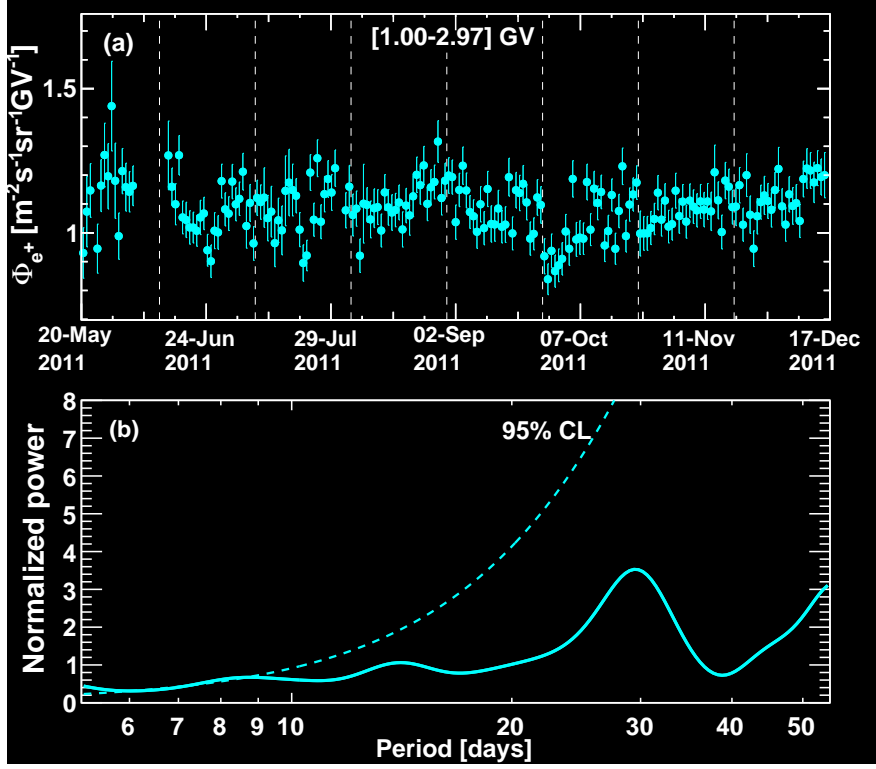


FIG. S5. (a)  $\Phi_{e^+}$  measured from May 20, 2011 to December 16, 2011 for the rigidity interval from 1.00 to 2.97 GV. Vertical dashed lines separate Bartels rotations. (b) Wavelet normalized power spectrum. The dashed curve indicates the 95% confidence level.

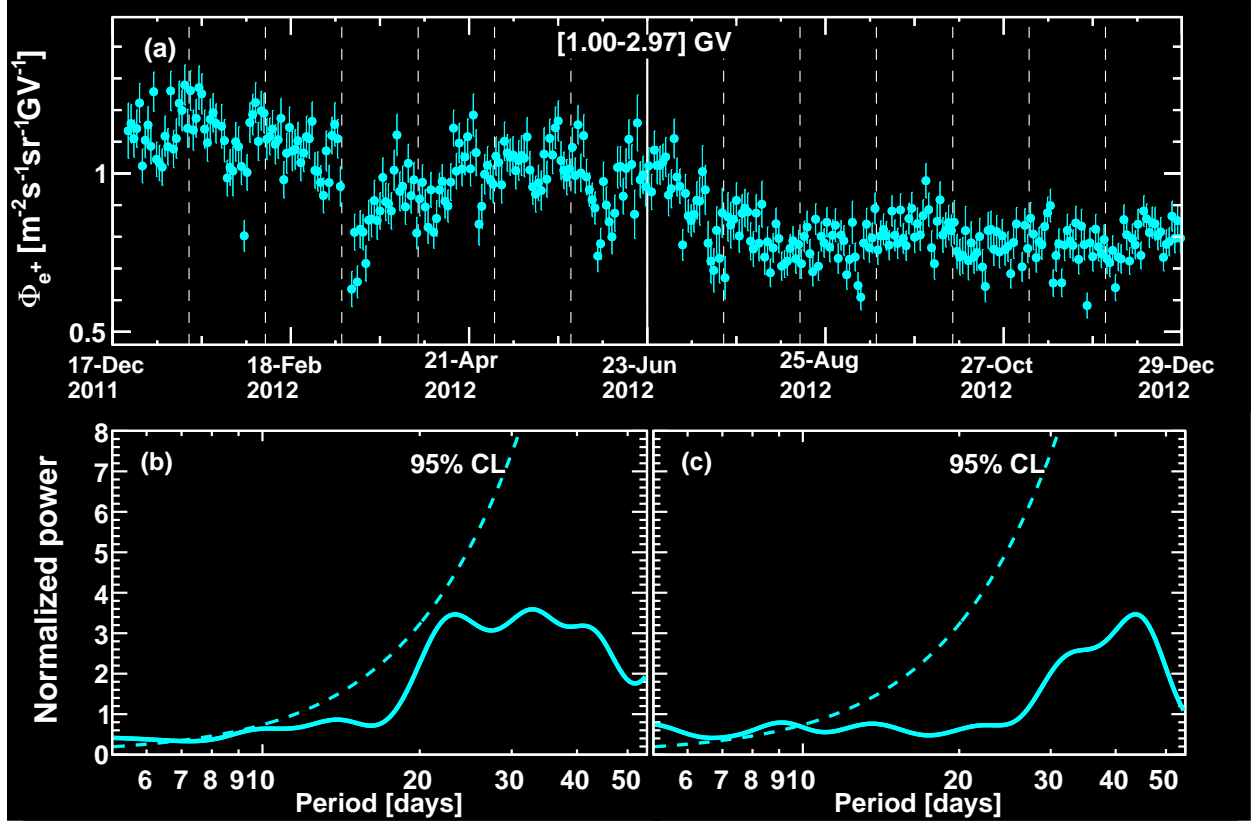


FIG. S6. (a)  $\Phi_{e^+}$  measured from December 17, 2011 to December 28, 2012 for the rigidity interval from 1.00 to 2.97 GV. Vertical dashed lines separate Bartels rotations. The vertical solid line separates two equal time intervals where the power spectra are calculated. (b,c) Wavelet normalized power spectra averaged (b) from December 17, 2011 to June 22, 2012 and (c) from June 23, 2012 to December 28, 2012. Dashed curves indicate the 95% confidence levels.

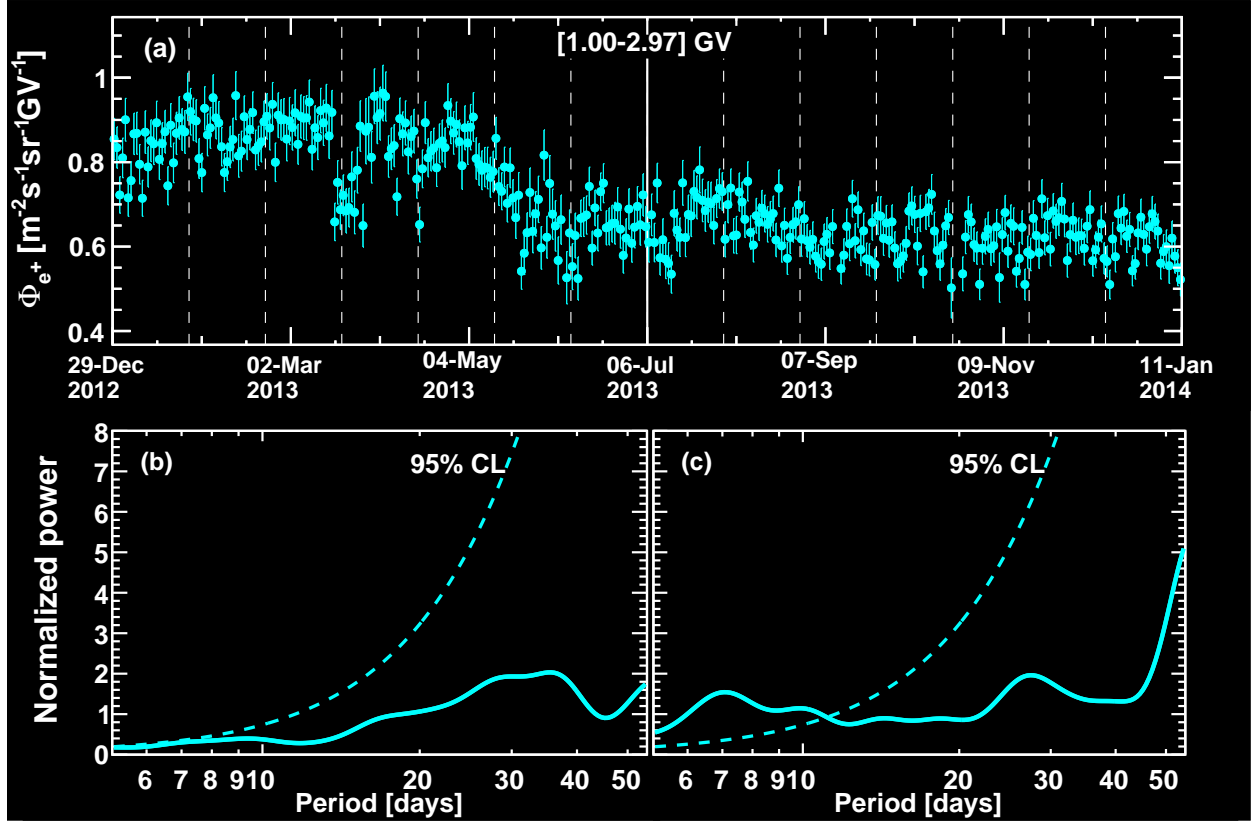


FIG. S7. (a)  $\Phi_{e^+}$  measured from December 29, 2012 to January 10, 2014 for the rigidity interval from 1.00 to 2.97 GV. Vertical dashed lines separate Bartels rotations. The vertical solid line separates two equal time intervals where the power spectra are calculated. (b,c) Wavelet normalized power spectra averaged (b) from December 29, 2012 to July 5, 2013 and (c) from July 6, 2013 to January 10, 2014. Dashed curves indicate the 95% confidence levels.

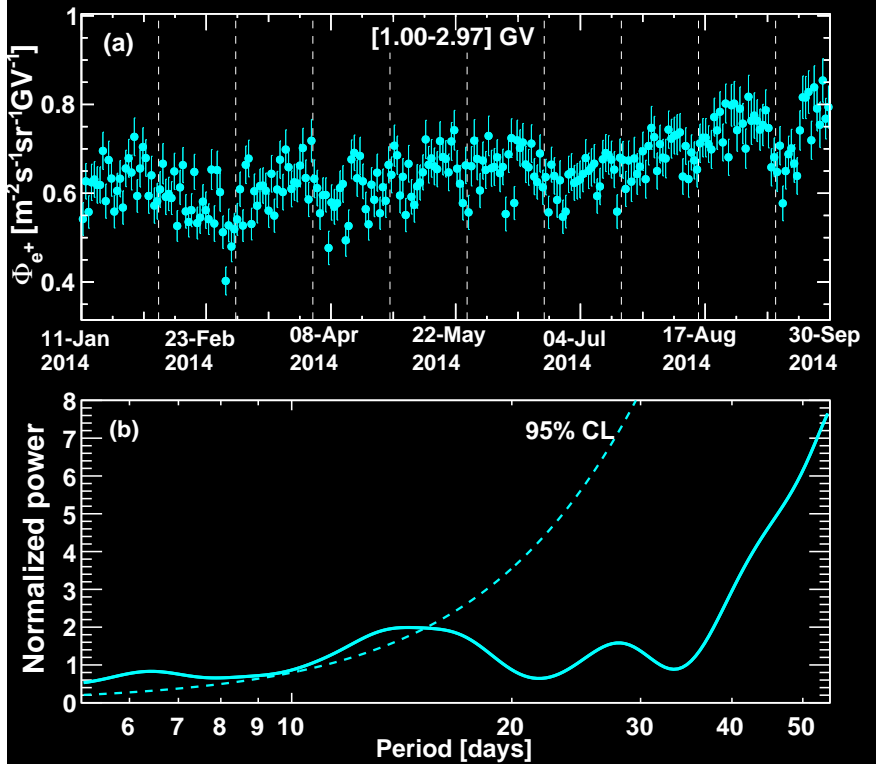


FIG. S8. (a)  $\Phi_{e+}$  measured from January 11, 2014 to September 29, 2014 for the rigidity interval from 1.00 to 2.97 GV. Vertical dashed lines separate Bartels rotations. (b) Wavelet normalized power spectrum. The dashed curve indicates the 95% confidence level. Note that in the time interval from September 30, 2014 to November 28, 2014, AMS was performing detector studies and no data was collected.

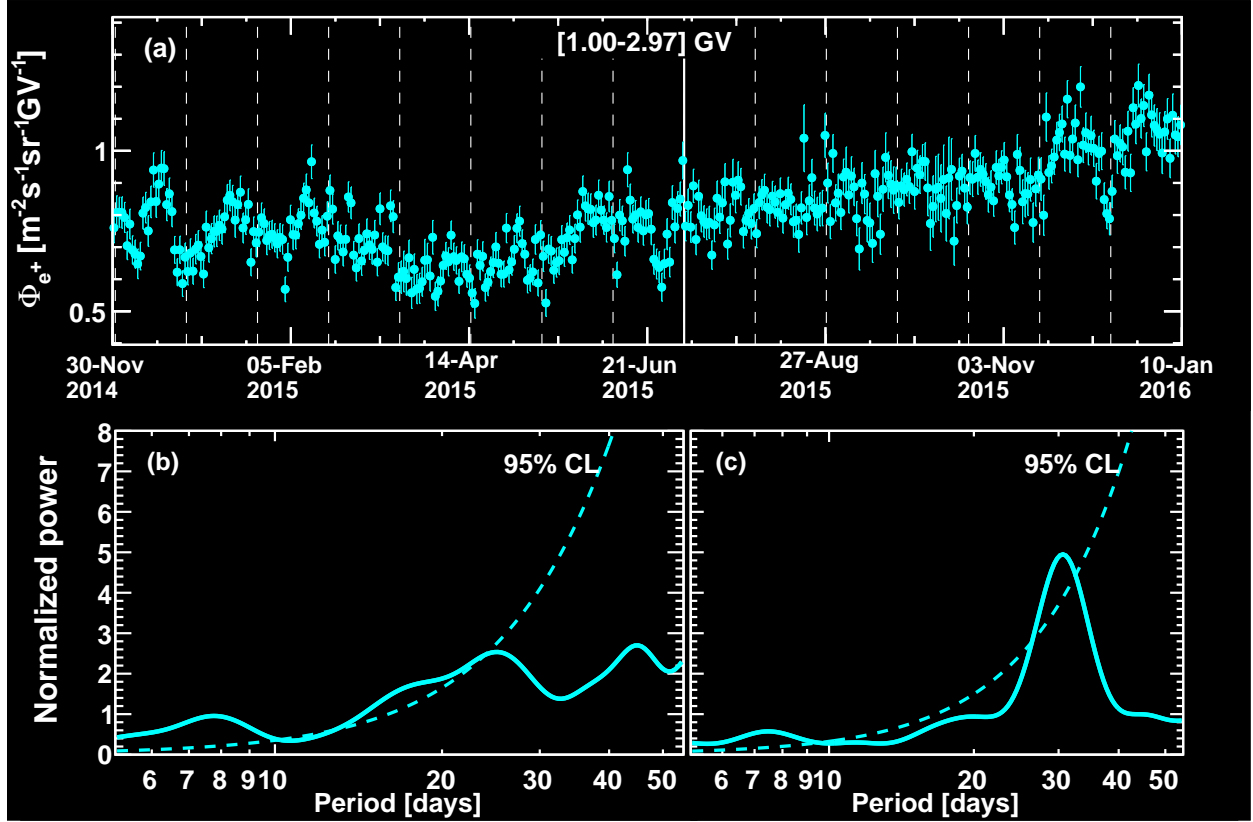


FIG. S9. (a)  $\Phi_{e^+}$  measured from November 29, 2014 to January 9, 2016 for the rigidity interval from 1.00 to 2.97 GV. Vertical dashed lines separate Bartels rotations. The vertical solid line separates two approximately equal time intervals where the power spectra are calculated. (b,c) Wavelet normalized power spectra averaged (b) from November 29, 2014 to July 4, 2015 and (c) from July 5, 2015 to January 9, 2016. Dashed curves indicate the 95% confidence levels.

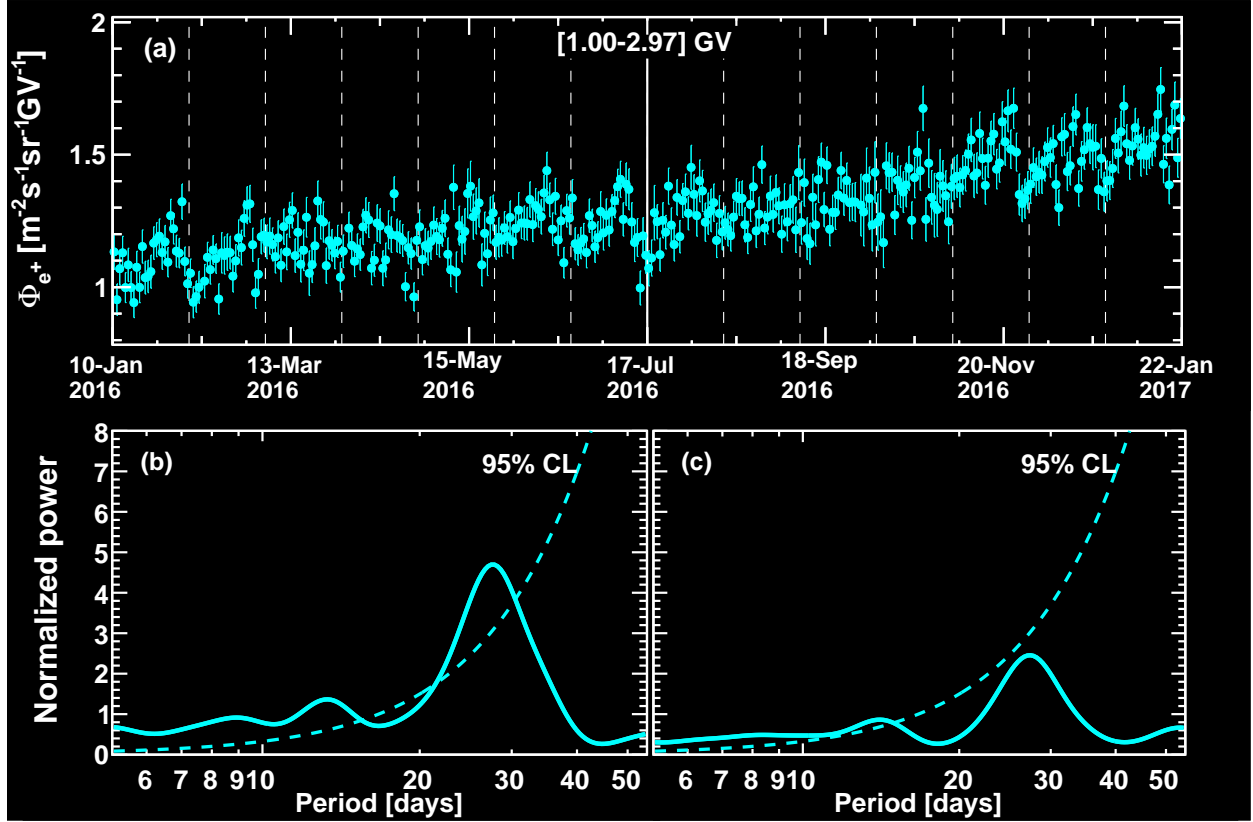


FIG. S10. (a)  $\Phi_{e+}$  measured from January 10, 2016 to January 21, 2017 for the rigidity interval from 1.00 to 2.97 GV. Vertical dashed lines separate Bartels rotations. The vertical solid line separates two equal time intervals where the power spectra are calculated. (b,c) Wavelet normalized power spectra averaged (b) from January 10, 2016 to July 16, 2016 and (c) from July 17, 2016 to January 21, 2017. Dashed curves indicate the 95% confidence levels.

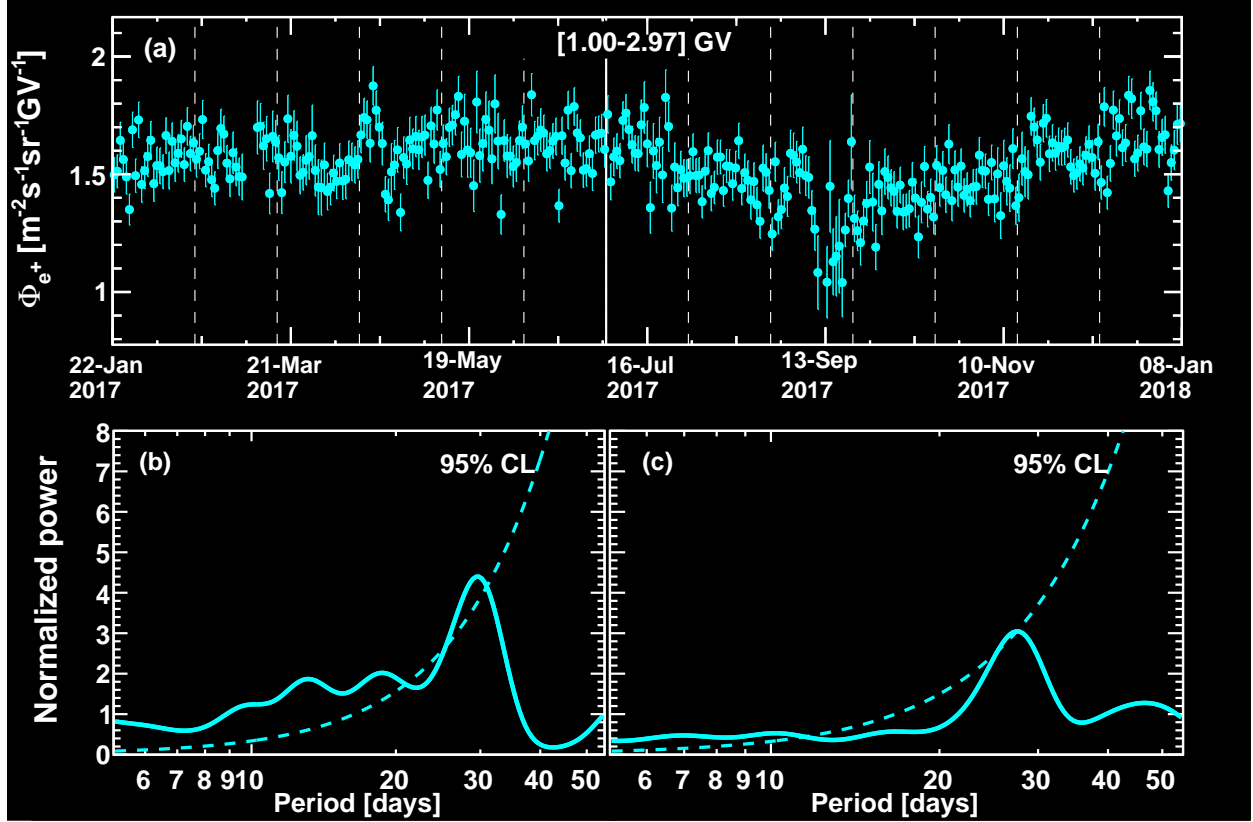


FIG. S11. (a)  $\Phi_{e^+}$  measured from January 22, 2017 to January 7, 2018 for the rigidity interval from 1.00 to 2.97 GV. Vertical dashed lines separate Bartels rotations. The vertical solid line separates two approximately equal time intervals where the power spectra are calculated. (b,c) Wavelet normalized power spectra averaged (b) from January 22, 2017 to July 2, 2017 and (c) from July 3, 2017 to January 7, 2018. Dashed curves indicate the 95% confidence levels.

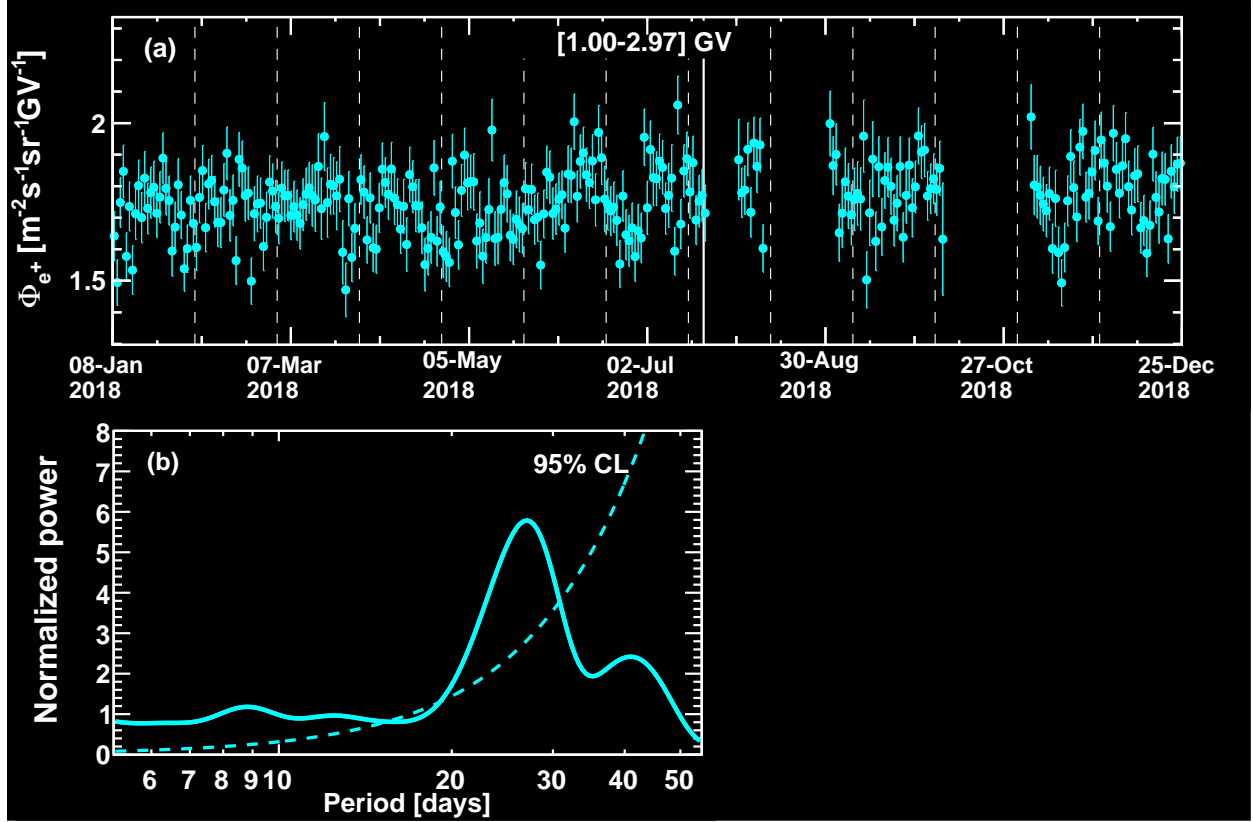


FIG. S12. (a)  $\Phi_{e^+}$  measured from January 8, 2018 to December 24, 2018 for the rigidity interval from 1.00 to 2.97 GV. Vertical dashed lines separate Bartels rotations. (b) Wavelet normalized power spectrum averaged from January 8, 2018 to July 20, 2018. The dashed curve indicates the 95% confidence level. Owing to interruptions in data taking due to the AMS upgrade, the data after July 20, 2018 is not included in the periodicity analysis.

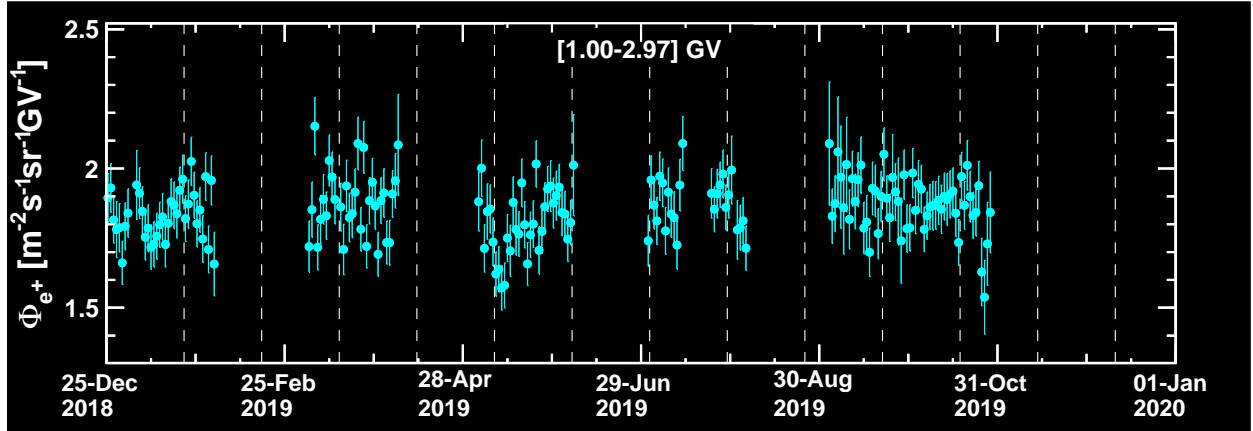


FIG. S13.  $\Phi_{e+}$  measured from December 25, 2018 to October 29, 2019 for the rigidity interval from 1.00 to 2.97 GV. Vertical dashed lines separate Bartels rotations. Owing to interruptions in data taking due to the AMS upgrade, the 2019 data is not included in the periodicity analysis.

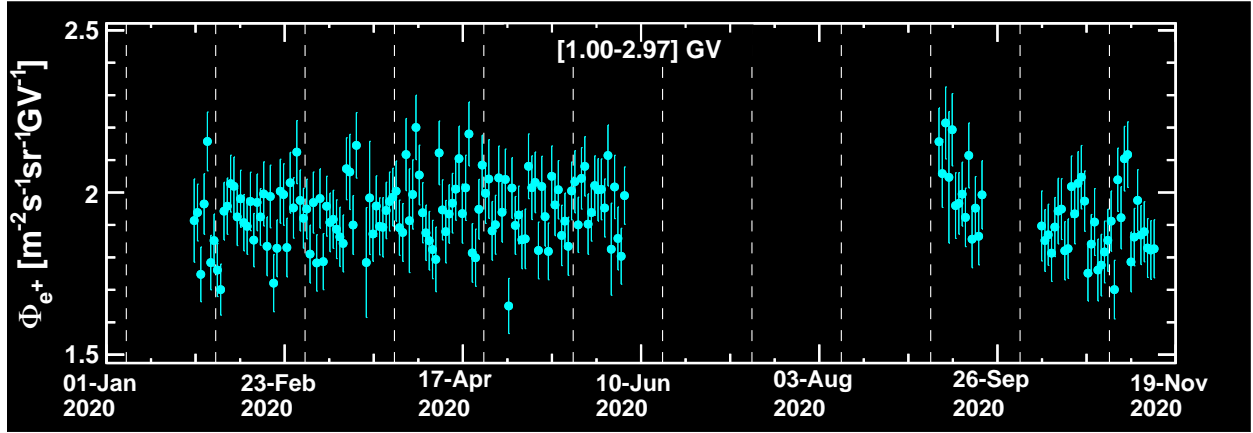


FIG. S14.  $\Phi_{e+}$  measured from January 26, 2020 to November 18, 2020 for the rigidity interval from 1.00 to 2.97 GV. Vertical dashed lines separate Bartels rotations. Owing to interruptions in data taking due to the AMS upgrade, the 2020 data is not included in the periodicity analysis.

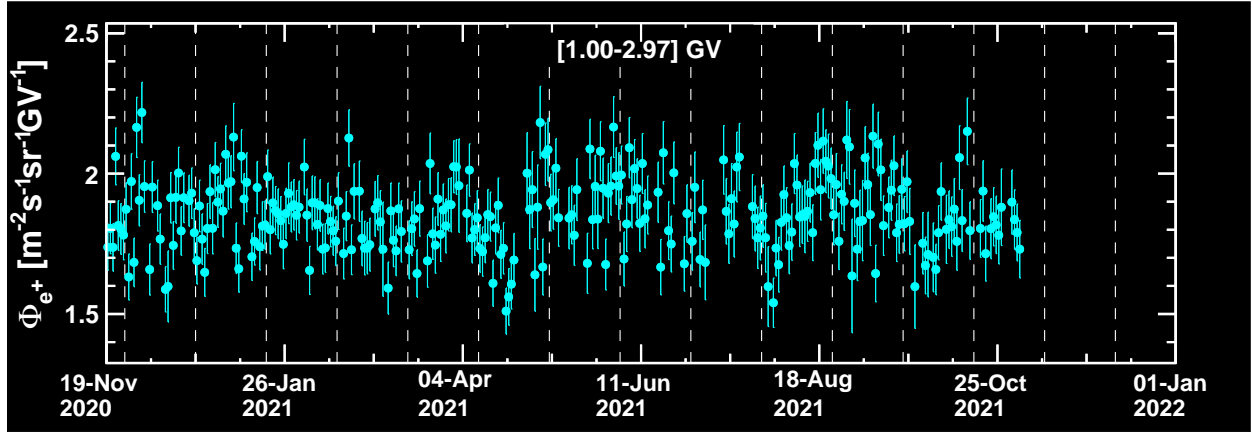


FIG. S15.  $\Phi_{e^+}$  measured from November 19, 2020 to November 2, 2021 for the rigidity interval from 1.00 to 2.97 GV. Vertical dashed lines separate Bartels rotations. Owing to interruptions in data taking due to the AMS upgrade, the 2021 data is not included in the periodicity analysis.

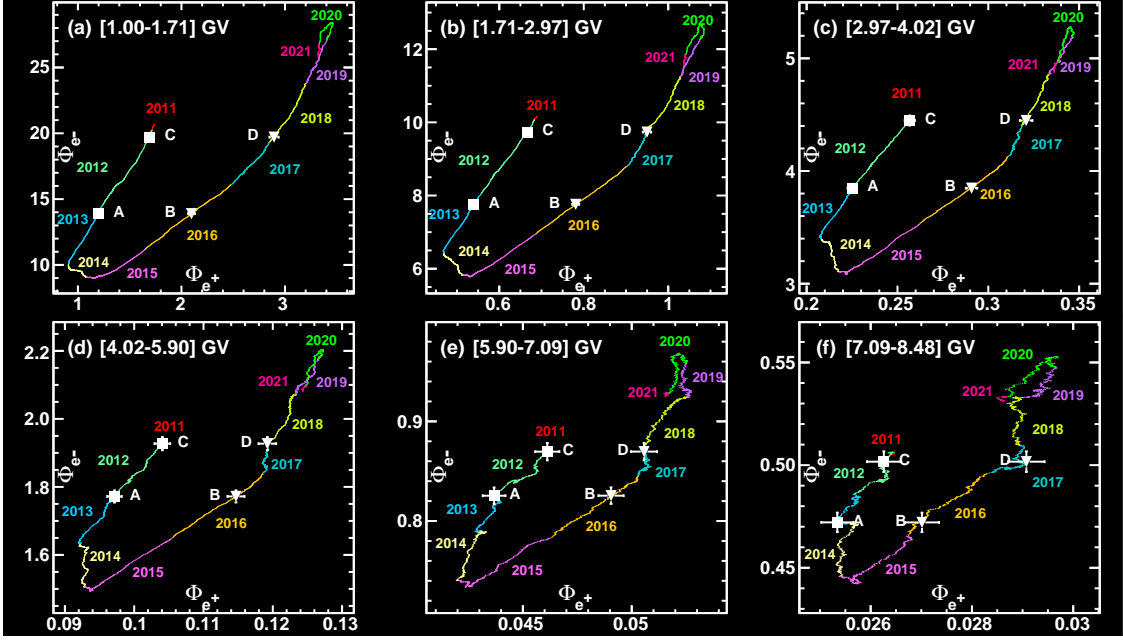


FIG. S16. The moving averages over 14 BRs and a step of 1 day of  $\Phi_{e-}$  versus  $\Phi_{e+}$ , both in units of  $[\text{m}^{-2}\text{sr}^{-1}\text{s}^{-1}\text{GV}^{-1}]$ , for six consecutive rigidity bins from 1.00 to 8.48 GV. Different colors indicate different years from 2011 to 2021. White squares (A and C) and white triangles (B and D) mark the two pairs of time intervals used to evaluate the significance of the hysteresis (see description in this Supplemental Material for details). The horizontal error bars are the quadratic sum of the statistical and time-dependent systematic errors of  $\Phi_{e+}$ . Vertical error bars are the quadratic sum of the statistical and time-dependent systematic errors of  $\Phi_{e-}$ .

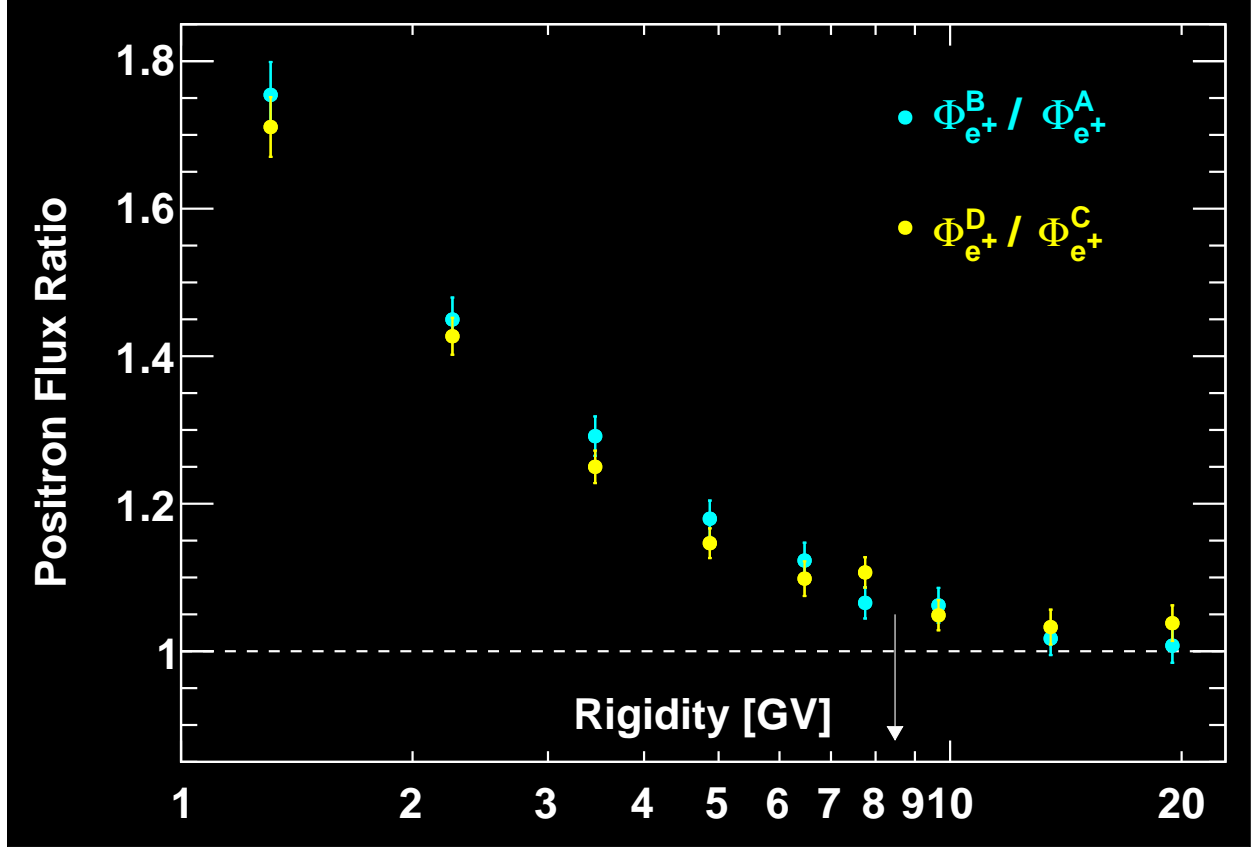


FIG. S17. The positron flux ratios  $\Phi_{e^+}^B / \Phi_{e^+}^A$  (light blue points) and  $\Phi_{e^+}^D / \Phi_{e^+}^C$  (yellow points) measured at two pairs of time intervals with the same  $\Phi_{e^-}$  as a function of rigidity from 1.00 to 22.8 GV (the first six rigidity bins are shown in Fig. S16). The error bars are the quadratic sum of the statistical and time-dependent systematic errors of  $\Phi_{e^+}$  and correlated errors from  $\Phi_{e^-}$ . The horizontal dashed line indicates unity.  $\Phi_{e^+}^B / \Phi_{e^+}^A$  and  $\Phi_{e^+}^D / \Phi_{e^+}^C$  deviate from unity with a combined significance greater than  $10\sigma$  at the first rigidity bin [1.00 - 1.71] GV and greater than  $5\sigma$  for each rigidity bin below 8.48 GV (indicated by the arrow).

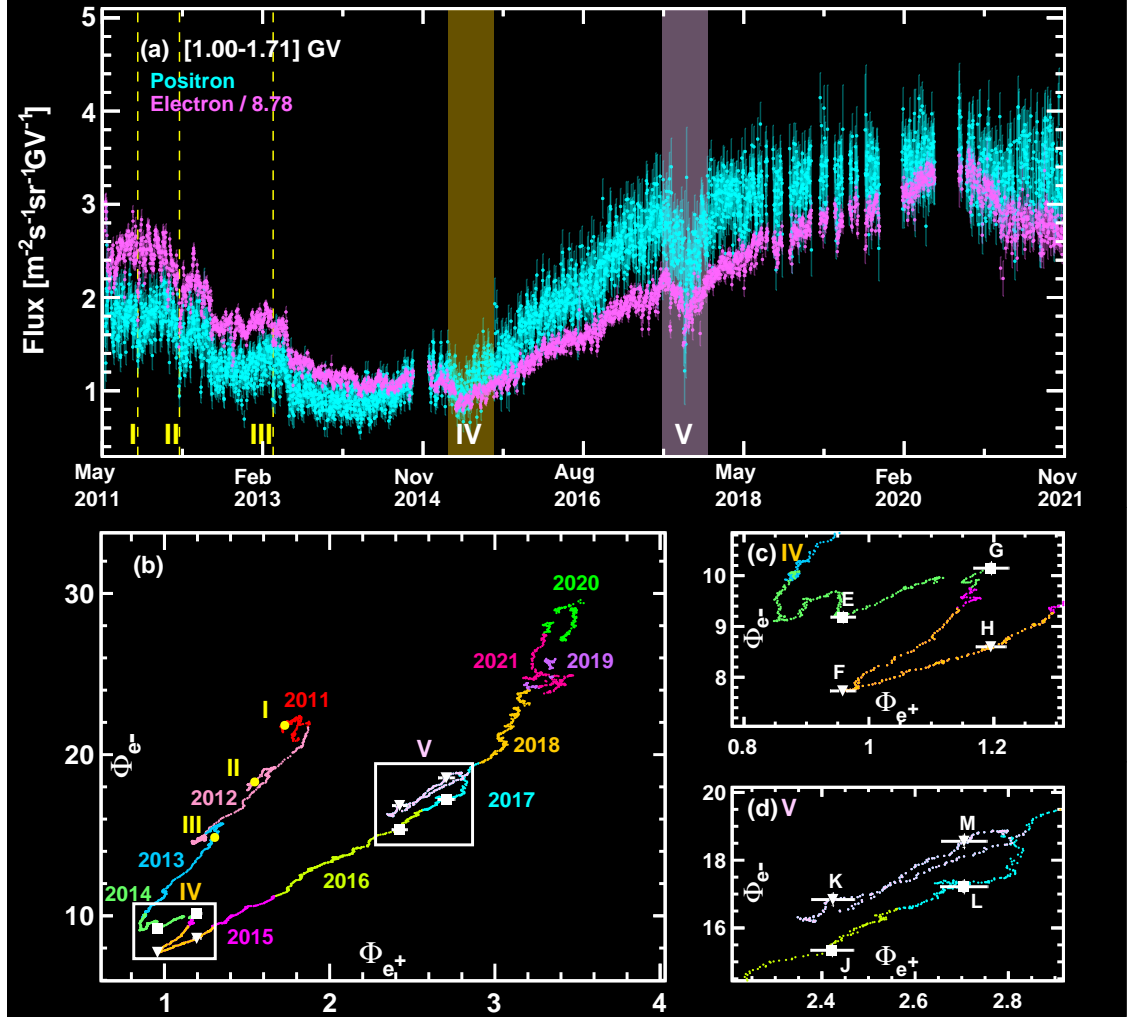


FIG. S18. (a) Daily  $\Phi_{e^+}$  (light blue points) together with daily  $\Phi_{e^-}$  (magenta points), measured for the rigidity interval from 1.00 to 1.71 GV over the entire period. For display purposes, the  $\Phi_{e^-}$  are divided by a scale factor such that  $\Phi_{e^+}$  and  $\Phi_{e^-}$  are at the same magnitude on average during 2014 and 2015. Dashed lines, I, II, and III indicate the location of sharp dips in  $\Phi_{e^+}$  and  $\Phi_{e^-}$ , and the colored bands IV and V mark the time intervals around the dips in 2015 and 2017. (b)  $\Phi_{e^-}$  versus  $\Phi_{e^+}$ , both calculated with a moving average of 2 BRs and a step of 1 day. Fluxes are in units of  $[\text{m}^{-2}\text{sr}^{-1}\text{s}^{-1}\text{GV}^{-1}]$ . Different colors indicate different years from 2011 to 2021. The location of I, II, and III correspond to the flux dips indicated in (a), and the white boxes IV and V to the time intervals around the dips in 2015 and 2017. (c) Detail of the structure in the time interval IV. White squares (E and G) and white triangles (F and H) mark the two pairs of time intervals used to evaluate the significance of the structure IV in the hysteresis (see description in this Supplemental Material for details). (d) Detail of the structure in the time interval V. White squares (J and L) and white triangles (K and M) mark the two pairs of time intervals used to evaluate the significance of the structure V in the hysteresis (see description in this Supplemental Material for details). The horizontal and vertical error bars are the quadratic sum of the statistical and time-dependent systematic errors of  $\Phi_{e^+}$  and  $\Phi_{e^-}$ , respectively.

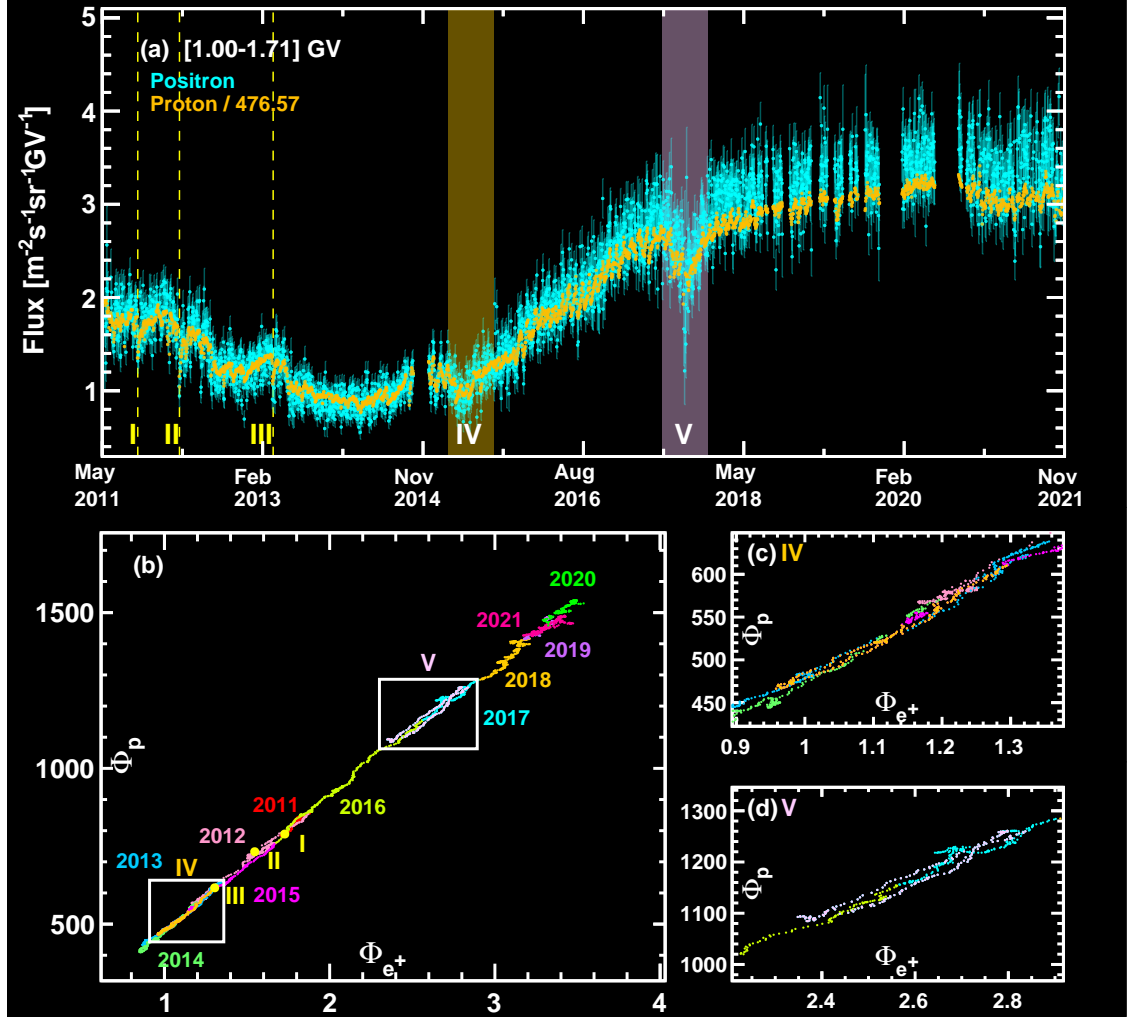


FIG. S19. (a) Daily  $\Phi_{e^+}$  (light blue points) together with daily  $\Phi_p$  (yellow points), measured for the rigidity interval from 1.00 to 1.71 GV over the entire period. For display purposes,  $\Phi_p$  are divided by a scale factor such that  $\Phi_{e^+}$  and  $\Phi_p$  are at the same magnitude on average during 2014 and 2015. Dashed lines, I, II, and III indicate the location of sharp dips in the  $\Phi_{e^+}$  and  $\Phi_p$ , and the colored bands IV and V mark the time intervals around the dips in 2015 and 2017. (b)  $\Phi_p$  versus  $\Phi_{e^+}$ , both calculated with a moving average of 2 BRs and a step of 1 day. Fluxes are in units of [m<sup>-2</sup>sr<sup>-1</sup>s<sup>-1</sup>GV<sup>-1</sup>]. Different colors indicate different years from 2011 to 2021. The location of I, II, and III correspond to the flux dips indicated in (a), and the white boxes IV and V to the time intervals around the dips in 2015 and 2017. (c) Detail of the  $\Phi_p$  to  $\Phi_{e^+}$  correlation in the time interval IV. (d) Detail of the  $\Phi_p$  to  $\Phi_{e^+}$  correlation in the time interval V. As seen, no significant structures are found.

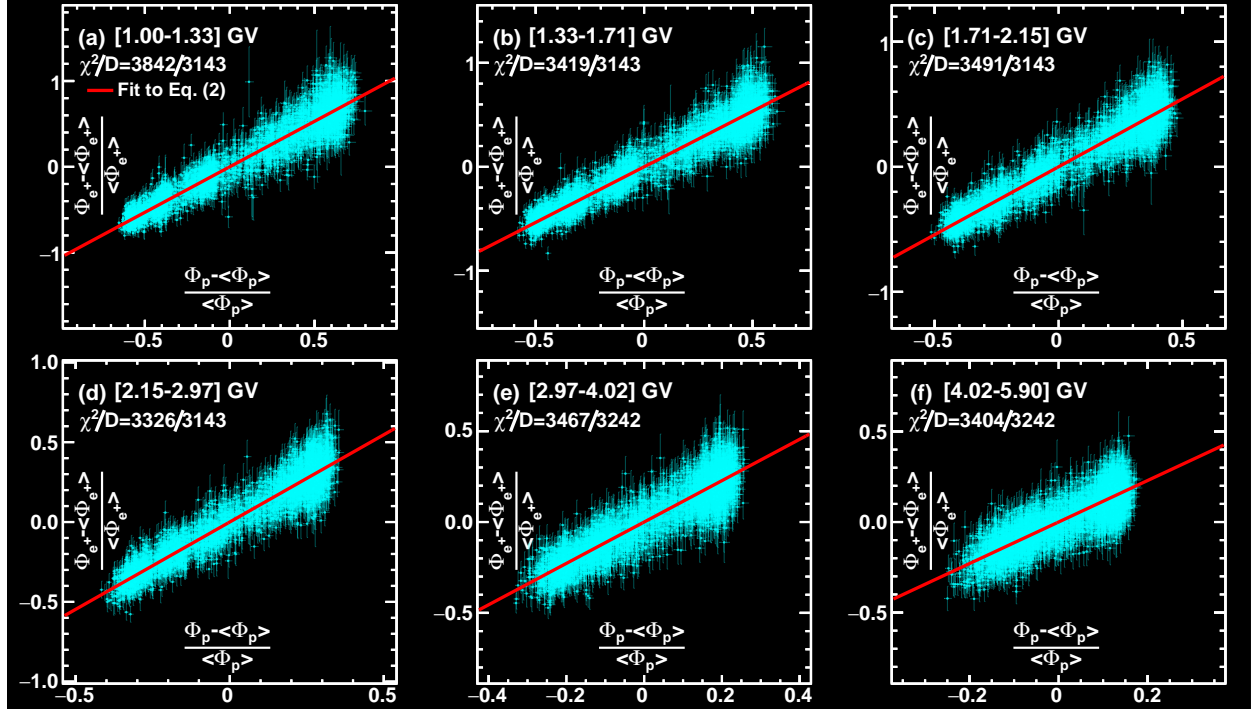


FIG. S20. The relative variation of the daily  $\Phi_{e+}$ ,  $\frac{\Phi_{e+} - \langle \Phi_{e+} \rangle}{\langle \Phi_{e+} \rangle}$ , versus the relative variation of the daily  $\Phi_p$ ,  $\frac{\Phi_p - \langle \Phi_p \rangle}{\langle \Phi_p \rangle}$ , for six consecutive rigidity bins from 1.00 to 5.90 GV. Days with Solar Energetic Particle events are excluded for rigidity bins below 3 GV. The horizontal and vertical error bars are the quadratic sum of the statistical and time-dependent systematic errors of  $\Phi_{e+}$  and  $\Phi_p$  respectively. The solid red line is the result of the fit of Eq. (2) to the data in each rigidity bin. The  $\chi^2$  per degree of freedom ( $\chi^2/D$ ) of the fits are also shown in the figure.